Quantitative Mass Spectrometry Imaging of Biological Systems

Daisy Unsihuay (dunsihua@purdue.edu), ORCID ID: 0000-0003-1638-3301

Daniela Mesa Sanchez (dmesasan@purdue.edu), ORCID ID: 0000-0002-4499-7872

Julia Laskin* (jlaskin@purdue.edu), ORCID ID: 0000-0002-4533-9644

Department of Chemistry, Purdue University, West Lafayette, Indiana, 47907, United States

*Corresponding author: jlaskin@purdue.edu

Keywords (up to 6): quantitative mass spectrometry imaging, matrix effects, protein imaging, lipids, drugs and metabolites

Abstract

Mass spectrometry imaging (MSI) is a powerful label-free technique, which provides detailed maps of hundreds of molecules in complex samples with high sensitivity and subcellular spatial resolution. Accurate quantification in MSI relies on a detailed understanding of matrix effects associated with the ionization process along with evaluation of the extraction efficiency and mass-dependent ion losses occurring in the analysis step. We present a critical summary of approaches developed for quantitative MSI (QMSI) of metabolites, lipids, and proteins in biological tissues and discuss their current and future applications.

1. INTRODUCTION

Mass spectrometry (MS) is a powerful analytical technique, which enables sensitive detection and identification of molecules in complex mixtures. With the advent of soft ionization techniques such as electrospray (ESI) (1) and matrix-assisted laser desorption ionization (MALDI) (2), MS became an indispensable tool for the label-free detection of intact biomolecules in biological samples. Dramatic improvements in the sensitivity, quantification, and identification capabilities of the MS instrumentation have uniquely positioned it at the forefront of biological research, clinical studies, drug discovery, forensics, and environmental sciences. Meanwhile, the development of approaches for the spatial localization of molecules using MS imaging (MSI) has extended these strengths of the analytical MS to the cellular and sub-cellular scale, and enabled detailed molecular mapping of hundreds of molecules in biological tissues (3–9).

Absolute quantification is one of the key challenges in the MS analysis of complex mixtures (10, 11). Aside from the instrumental parameters and sample preparation protocols, quantitative MS must address the complexity associated with dramatic variations in the ionization efficiency of different classes of compounds, signal suppression during ionization of complex mixtures also referred to as “matrix effects”, and the lack of appropriate standards (11). Relative quantification relies on an internal standard or a selected endogenous molecule in the sample to access the relative change in concentrations of other molecules in different samples. This approach is commonly used in untargeted profiling of the variations in the chemotype of a system at different conditions. Meanwhile, absolute quantification provides the absolute values of concentrations of analytes in the sample making it much more challenging, in particular in the context of complex mixture analysis of interest to this review.

A majority of quantitative MS studies of small molecules involve separation such as liquid or gas chromatography (LC or GC), which reduces the complexity of the analyte mixture. These studies typically rely on targeted techniques, in which isotopically labeled standards are used to convert peak abundances observed in mass spectra into concentrations. In quantitative metabolomics (12, 13), the scarcity of standards may be addressed by employing microbial metabolism to generate libraries of isotopically labeled biomolecules. However, this approach still requires a substantial investment into the calibration and validation of the newly designed libraries of standards. In lipidomics (14), quantification typically utilizes two standards per lipid class, which are selected from lipid species expected to be absent in a specific system under investigation. Correction factors are established to account for the differences in the ionization efficiency of lipids with different length and degree of unsaturation of the fatty acyl chains (15). Several experimental approaches have been developed for the absolute quantification in proteomics experiments. These techniques will not be discussed here and the readers are referred to several excellent reviews on this topic (16, 17).

Since the initial demonstration of MSI by the Caprioli group (18), MALDI has become the most widely used soft ionization technique in MSI experiments with several commercial platforms available to the scientific community (8, 9, 19, 20). Recent developments of ambient ionization techniques, in which samples are analyzed without special pre-treatment, have expanded the range of MSI applications (21–23). These ionization techniques can be classified into laser-based and liquid extraction-based approaches (24). Laser ablation (LA) and LA coupled with ESI (LAESI) (25) along with matrix-assisted laser desorption ESI (MALDESI) (26) are among the most widely used laser-based ionization techniques in MSI. Meanwhile, a majority of MSI experiments involving liquid extraction-based techniques have relied on desorption electrospray ionization

(DESI) (27, 28) and its variants along with nanospray desorption electrospray ionization (nano-DESI) (29), liquid microjunction surface sampling probe (LMJ-SSP) (30), and liquid extraction surface analysis (LESA) (31).

Regardless of the ionization technique employed, MSI experiments always involve simultaneous analysis of hundreds of molecules extracted from each location on the sample without a chromatographic separation or sample clean-up. Furthermore, the addition of the standards in MSI experiments is not straightforward. As a result, many quantification strategies developed for bulk sample analysis using MS cannot be directly applied to MSI. Despite these challenges, several approaches have been developed to facilitate quantitative MSI (QMSI). In this review, we will focus on the most recent developments in QMSI. Earlier studies in this field have been previously reviewed (32–35). We present approaches for QMSI of metabolites, lipids, and proteins in biological tissues and discuss their current and future applications.

2. MATRIX EFFECTS IN MSI

Matrix effects are common in MSI experiments (36, 37). The extent of signal suppression varies with the composition of the analyzed mixture. In tissue imaging, changes in the chemical composition of species extracted from different anatomical regions of heterogeneous tissue sections is the key factor determining the severity of matrix effects. Two types of matrix effects have been observed in MSI experiments: 1) ionization suppression due to the competition of molecules for charge and 2) signal enhancement or suppression due to variations in the alkali metal concentrations in different regions of the tissue sample. Severe matrix effects were observed in nano-DESI MSI of lipids, drugs, and neurotransmitters in murine brain tissues (36, 38, 39). Regardless of their origin, matrix effects may affect the observed spatial localization of molecules

and thereby quantification of their concentrations in different parts of the tissue sample. It follows that compensation for matrix effects is necessary for the accurate quantification in QMSI experiments.

2.1 Normalization strategies

Different normalization strategies have been developed to compensate for matrix effects. Normalization of ion signals to the total ion current (TIC) is the most widely used approach in MSI experiments. It has been demonstrated that signal variations due to matrix effect are retained in ion images normalized to the TIC. For example, Lanekoff et al. used a mouse brain tissue of a middle cerebral artery occlusion (MCAO) stroke model to illustrate the different types of matrix effects observed in MSI of complex biological samples (36). In this experiment, nano-DESI MSI was performed using a solvent containing two phosphatidylcholine (PC) standards, PC 25:0 and PC 43:6, supplied at a constant rate throughout the experiment. An optical image of the MCAO brain tissue section and ion images of both endogenous PC species and PC 43:6 standard normalized to the TIC and to the signal of an appropriate adduct of PC 25:5 are shown in **Figure 1**. The distribution of the signals of the sodium and potassium adducts of the standard shown in **Figure 1** are clearly not uniform indicating the presence of matrix effects. First, suppression of potassium adducts and enhanced signals of sodium adducts of the same analyte molecules is observed in the ischemic region of the brain. This is attributed to differences in alkali metal concentrations caused by ischemia. Second, the high content of glycolipids in the white matter and the low ionization efficiency of these molecules results in an enhanced signal intensity of the PC standards in this region of the brain. These results demonstrate that normalization to the TIC cannot be used to compensate for these types of matrix effects.

Normalization to the standard has been used to generate ion images free of matrix effects as shown in **Figure 1**. In this approach, the signals of endogenous PCs are normalized to the corresponding adduct of the PC standard. It has been demonstrated that normalization to the signal of the standards is a promising strategy for obtaining accurate concentration gradients in MSI of tissue sections. Multiple standards may be used to assess matrix effects for different classes of lipids and metabolites observed in MSI experiments.

Several studies used normalization over a region of interest instead of pixel-by-pixel normalization to compensate for regional matrix effects. In this approach, a tissue extinction coefficient (TEC) is used as a normalization factor to obtain normalized abundances of endogenous molecules extracted from the tissue. TEC is generally used to evaluate the analyte ion suppression across different regions within the tissue or across different type of tissues. In one study, region-specific matrix effects were examined for a drug, olanzapine, which was evenly deposited onto a mouse brain tissue (40). The authors used the graph-cuts algorithm to automatically cluster pixels from areas corresponding to different anatomical regions of the brain and calculated region-specific TEC values shown in **Figure 2a**. Direct comparison of the results obtained in DESI and MALDI experiments showed a 4-fold decrease in TEC values in MALDI in comparison with DESI indicating that olanzapine experienced higher ion suppression in MALDI experiments. Normalization of olanzapine signals to region-specific TEC values shown in **Figure 2b**, largely eliminates regional ionization suppression effects and enables alignment of normalized intensities across clusters corresponding to different anatomical regions. Ion images of olanzapine are shown in **Figure 2c**. When normalized to the TIC, olanzapine shows higher signals in the white matter indicating the presence of matrix effects. However, ion images normalized to TEC show a more uniform distribution of olanzapine across the tissue, which is consistent with the expected

distribution of the deposited drug. It has been demonstrated that the performance of this approach is highly dependent on the number of clusters used for the normalization; the characteristic anatomical features are still visible with 15 clusters (**Figure 2c**) and are less prominent with 50 clusters (not shown).

2.2 Experimental approaches

Other strategies, which help reduce matrix effects in MSI typically rely on sample preparation to obtain a better control of the ionization process. Spraggins et al. examined the effect of matrix application approach and the properties of the matrix on the sensitivity of MALDI MSI towards different lipids using mouse liver tissue (41). Matrix selection affects the observed molecular profiles, types of adducts, and lipid coverage obtained using MALDI. For example, protonated species are more abundant when 1,5-diaminonaohtalene (DAN) and 9-aminoacridine (9AA) are used as matrices. Meanwhile, 2,5-dihydroxybenzoic acid (DHB), 5-chloro-2-mercaptonezothiazole (CMBT), and 2,5-dihydroxyacetophenone (DHA) facilitate the formation of alkali metal adducts of analytes with potassium adducts preferably formed when DHA in used as a matrix. Matrix application method mainly affects the types of adducts generated in the ionization process. Alkali metal adducts are preferentially formed when the matrix is applied using spray-coating, whereas matrix sublimation onto the tissue favors the formation protonated molecules. This study demonstrated that better understanding of the physicochemical processes occurring at the tissue-matrix interface is important for controlling molecular profiles observed in MALDI MSI. We note that matrix effects should not be confused with the effect of the matrix in MALDI experiments. However, understanding of the effect of the matrix provides important insights into the origin and extent of matrix effects in MALDI MSI.

Different matrices have been examined to enhance the sensitivity of low-abundance analytes for accurate quantification. For example, Yang et al. found that α-cyano-4-hydroxycinnamic acid (CHCA) matrix was best-suited for the detection of an environmental organic pollutant, perfluorooctanesulfonic acid (PFOS) in mouse kidney (42). PFOS was preferentially detected in negative mode, likely due to its acidity ($pK_a < 1$), and with highest intensity in CHCA matrix among all other surveyed matrices. Likewise, Rzagalinski et al. used a (2-[(2E)-3-(4-tert-butylphenyl)-2-methylprop-2-enylidene]malononitrile) (DCTB) matrix to improve the sensitivity of MALDI towards five central nervous system drugs, xylazine, imipramine, clozapine, ketamine, and clonidine (43). Although standards of all five drugs alone exhibited the highest signal intensities when CHCA was used as a matrix, DCTB was a preferred matrix for the analysis of the standards mixed with brain tissue homogenate. The increased signal suppression by CHCA was evaluated by calculating the TEC values, which showed an 8-fold larger suppression factor by the CHCA matrix than the DCTB matrix. For the quantification of xylazine in mouse brain, this difference represented nearly 100-fold signal intensity increase in single pixels and upwards of 400-fold increase in ion abundances observed using DCTB in comparison with CHCA matrix. Despite DCTB being traditionally considered an electron transfer matrix, the calculated gas-phase proton affinity of DCTB of 866 kJ/mol is similar to that of CHCA (863 kJ/mol) and significantly lower than those of the studied drugs: xylazine (1018 kJ/mol) and ketamine (964 kJ/mol). Therefore, it is reasonable to assume that proton transfer from protonated matrix molecules to the desorbed analytes may be responsible for the efficient detection of this series of drugs using DCTB.

Ionization suppression of small metabolites can be reduced using matrix additives. Ammonium sulfate (AS) has been used as a matrix additive to improve the signal from hydrophilic quaternary ammonium compounds such as carnitine, acetylcarnitine and phosphocholine (44). These

compounds are generally suppressed in MALDI experiments due to the presence of more readily ionizable molecules. A properly selected matrix additive helps bring up the signal of these compounds by suppressing the signals of more abundant species including PCs and clusters derived from the DHB matrix. In the presence of 63 mM AS in the matrix, MALDI favors the formation of protonated species and suppresses the formation of alkali adducts. Such high concentrations of AS are believed to cause "salting out" of several classes of molecules, which reduces their solubility. In contrast, quaternary ammonium compounds are efficiently extracted and co-crystalized with the DHB matrix in the presence of AS. Although the molecular coverage obtained using this approach is substantially reduced, five quaternary ammonium compounds, which have not been observed using other matrices, could be spatially localized by adding AS to the matrix.

On-tissue derivatization strategies have been explored for QMSI of low ionization efficiency compounds using MALDI. For example, Barré et al. used Girard's reagent T (GT) to derivatize triamcinolone acetonide (TAA), an osteoarthritis drug, which is otherwise nearly undetectable with ESI or MALDI (45). In this study, the tissue coated with GT was incubated for 2.5 h at 40 °C prior to analysis. This strategy was used to quantify and visualize the spatial distribution of TAA. Derivatization resulted in a 78-fold increase in the TAA signal and allowed to quantify the penetration of TAA into cartilage. A homogenous distribution of TAA in the cartilage was observed after a 48 h incubation with the drug.

Similarly, ambient liquid extraction-based techniques have exploited different strategies to improve both the extraction and ionization efficiency of targeted molecules. It has been demonstrated that solvent composition may be optimized to improve analyte extraction based on its polarity. For example, methanol/water mixtures are commonly used for the extraction of polar

molecules whereas solvents containing non-polar components are used to improve the solubility of less polar molecules (46). In DESI experiments, dimethylformamide has been used to preserve the morphological structure of tissue sections (47). The ionization efficiency of poorly ionizable molecules may be improved using ionization enhancers that facilitate cationization of analytes generally detected in negative mode. This approach has been used for imaging of prostaglandins using complexation with Ag^+ (48) and phosphoethanolamines by forming a complex with a synthetic dication (DC9) (49). Online derivatization also has been used to improve the sensitivity of ambient ionization techniques towards neutral molecules. For example betaine aldehyde selectively reacts with alcohol groups, which enables imaging of neutral sterols (50).

3. QMSI OF SMALL BIOMOLECULES IN TISSUES

Differences in sample preparation for imaging experiments necessitate different QMSI approaches for imaging of small biomolecules (e.g. lipids, metabolites, drugs, and other) in tissue sections. In the following, we will discuss these approaches separately for several classes of ionization techniques.

3.1 MALDI and Related Techniques

Quantitative strategies for MALDI and other related laser-based techniques are dominated by two main approaches: on-tissue spotting of standards and mimetic models (51). A third "in-solution" approach, in which standards are applied to an off-tissue region and correlated using the TEC factors, exists but has largely fallen out of fashion in recent years. In each approach, several concentrations of a standard (often an isotopically-labeled analog of the target analyte) are used to generate a standard curve that can then be utilized to correlate ion signals observed in imaging

experiments to known concentrations values. However, both the on-tissue spotting, and the mimetic model approaches require significant sample preparation, which we discuss below.

3.1.1. On-tissue spotting of standards

On-tissue spotting is performed using one of the four methods illustrated in **Figure 3**: 1) spotting of the standard directly on top of tissue followed by matrix application; 2) spotting of the standard directly on the glass slide, followed by mounting of the tissue, and subsequent matrix application; 3) spotting using a sandwich method in which half of the standard is applied directly on the glass followed by tissue mounting and spotting of the other half of the standard on top of this tissue prior to matrix application; 4) incorporation of the standard into the matrix itself. Chumbley et al. compared these methods using a drug, rifampicin, in liver tissue (52). Although quantification values for all the techniques were comparable, the first method, in which the standard is spotted directly on top of the tissue, produces quantitative values most consistent with HPLC-MS/MS results from a dosed tissue homogenate. Meanwhile, premixing the standard with the matrix produced somewhat lower concentrations. Although the origin of this effect has not been thoroughly investigated, the partitioning of the analyte into the crystals may be affected by the presence of a similar molecule already uniformly premixed with the matrix. Alternatively, co-crystallization of the standard and matrix on the tissue may enhance its ionization efficiency. Subsequently, the standard is preferentially ionized whereas the analyte is only partially extracted in comparison. This results in lower calculated concentrations of the analyte upon normalization. Conversely, application of the standard under the tissue or partly under the tissue in the sandwich method results in concentrations higher than the ones obtained using HPLC-MS/MS, and, furthermore, introduces greater experimental variability. This is attributed to the inconsistent or

poor penetration of the standard through the tissue for subsequent extraction into the matrix crystals, and thereby a lower than expected abundance of the standard.

3.1.2 Mimetic tissue model

Similar to the on-tissue QMSI strategy, the mimetic model approach requires prior sample preparation. Several mimetic tissue preparation protocols have been developed to ensure accurate quantification in QMSI experiments. Generally, these protocols utilize homogenate mixtures of the target tissue spiked one or more standards at different concentrations. It is assumed that the signal of the standard observed in the analysis of such tissue homogenate adequately represents matrix effects experienced by the appropriate analytes examined in QMSI experiments (53). Although the use of tissue homogenate cannot be used to evaluate differences in matrix effects in different anatomical regions of the analyzed tissue, it facilitates accurate quantification for systems, in which such effects are not particularly pronounced.

A mimetic tissue preparation protocol shown in **Figure 4** utilizes serially frozen spiked-tissue homogenate layers in a cylinder to create a single cross-section with a concentration gradient that can be mounted along with the experimental tissue for easier analysis (54). Special care is taken to minimize the spiked standard solution volume (in this case, clozapine below 3% w/w) to maintain native tissue density. Mimetic models for liver, kidney, and brain tissue mimics have been prepared, but only liver and brain models were validated using LC-MS, resulting in 1.5% and 2.1% error, respectively. Another recent methodology for mimetic model construction incorporates native cells, and a hydrogel scaffold component in addition to tissue homogenate to generate a 3D biomimetic tissue (55). To do this, tissue is homogenized in the presence of a 2.5% agarose saline solution, spiked with the appropriate standard, combined with a concentrated organ-derived cell suspension, and left to set for 10 to 15 minutes. The reincorporation of native cells,

which do not survive the homogenization process might better replicate the native tissue structural integrity. The relative deviation between ionization efficiencies of a spiked drug for this model tissue and the real tissue was less than 15%, though no comparison is made to other spiked-homogenate protocols.

3.1.3 Examples of QMSI applications

Both on-tissue spotting and mimetic model strategies have been used in many applications, some of which are described here. Giordano et al. used an on-tissue approach to better understand the role of structural heterogeneity and tumor microenvironment by quantifying the drug penetration of paclitaxel in a malignant pleural mesothelioma tumor model via a 3D imaging experiment (56). This imaging experiment analyzed multiple sequential sections from the same tumor, which were then computationally reconstructed into a 3D model to visualize the paclitaxel penetration. Predictably for malignant pleural mesothelioma, a highly heterogenous neoplasm with high resistance to drugs, paclitaxel was primarily concentrated on the tumor edges or in about only 0.21% of the tumor volume. The remaining paclitaxel was found at low concentrations (<0.2 μg/g, below the limit of detection) in 37.7% of the tissue volume. Notably, this experiment showed paclitaxel in higher concentrations in and around non-necrotic areas, and in low concentration around fibrotic and necrotic regions of the tumor. This finding corroborates the hypothesis that hypoxic tumor areas are especially difficult for chemotherapeutics to reach, and thus may be the sites of tumor resistance and reemergence.

Nazari et al. used the on-tissue approach to quantify an endogenous metabolite, glutathione (GSH) in hen ovarian tissue using a related laser-based technique, IR-MALDESI (57). In this experiment, age-matched healthy and cancerous tissues were compared and a dilution series of stable isotope labeled GSH pipetted on top of tissue was used to generate a calibration curve. An

acute increase in GSH concentration was observed in cancerous tissue, and a heterogenous distribution was seen in both tissue types. Although the absolute GSH concentrations calculated from the IR-MALDESI experiment were twice higher compared to LC-MS/MS, the approximate 2-fold change between healthy and cancerous tissue was consistent between both techniques.

GSH in human ocular lens was quantified using a mimetic model to better understand the aging-related development of lens cataract formation (58). Four donor tissues, ranging in age from 29 to 82, were analyzed. GSH was found to decrease with increasing age, primarily in the nucleus. However, some biological variability was noted with the lowest GSH concentrations present in the second-oldest age sample (74 yrs, 2.7 μmol/g tissue in cortex, and 0.8 μmol/g in the nucleus). These values are in agreement with the average literature values generated using alternative quantitative techniques. To further validate the use of a homogenous mimetic model for quantification of GSH in different regions of the lens, ion suppression between cortex and nucleus was tested and found to be minimal (approx. 3%). This study also examined other small metabolites, including ceramides which localized in areas of lowest GSH concentration, and showed a signal increase with decrease in nuclear GSH.

The repeatability and reproducibility of QMSI based on mimetic models was examined for the quantification of the drug clozapine and its major metabolite norclozapine in perfused rat liver (59). Despite some differences in the sampling regions utilized for QMSI and LC-MS/MS analyses, this study found an 84% and 82% accuracy in the quantification of clozapine and norclozapine, respectively, in comparison to LC-MS/MS. Accuracy was determined from the mean of pooled MSI data acquired by three different analysts, six replicates (serial tissue sections) each, at three separate locations, while LC-MS/MS analysis was done at the same site. The repeatability of the technique was determined by the intra-analyst precision (% relative standard

deviation, RSD) and was found to be 12% for both clozapine and norclozapine upon normalization to an isotopically labeled standard, clozapine-d8. However, unnormalized values were 8% and 7% for clozapine and norclozapine, respectively, which more closely matched the 8% RSD of LC-MS/MS analysis. Reproducibility was described by pooling of all the replicates examined by the three analysts. For clozapine, reproducibility was 13% and 14% for normalized and unnormalized values, respectively. However, for norclozapine reproducibility significantly worsened when normalized to the standard, 27%, compared to the raw value of 13%. The slight worsening in accuracy and substantial worsening in reproducibility upon normalization could be attributed to differences in the extraction efficiency of analytes from the heterogeneous tissue matrix in comparison to the homogeneously surface-coated standard. This results in an exaggerated correction by normalization and thereby largely mismatched variances. This phenomenon has been previously investigated, but the general recommendation is that normalization to a standard is best used when the ratio of analyte and standard signal is close to unity. In general, the low values of RSD reported in this study are an encouraging result towards the validation of MALDI QMSI.

3.1.4 New experimental approaches

Several studies have highlighted important experimental considerations in MALDI QMSI beyond the sample preparation strategies. For example, Porta et al. optimized laser energy and sample stage velocity to avoid analyte carryover and minimize intra-spot variability, respectively (34). Moreover, the authors examined the effect of the frequency and number of laser shots per pixel on the intra-spot variability and, therefore, accuracy of quantification. This study demonstrated that an average of 4-5 pixels is best suited for accurate quantification, such that instrumental variability and matrix heterogeneity are confidently accounted for.

Abundant matrix peaks in the low *m/z* range present a challenge for MALDI QMSI of small biomolecules, which is typically addressed using MS/MS. A high-speed TOF/TOF system has been used to acquire multiple TOF/TOF events in a single laser shot (60, 61). This technique enables the acquisition of MS/MS spectra of both the analyte and standard in the same laser shot, which enables normalization of the analyte signal to the signal of the standard in each pixel and thereby reduces signal variability in QMSI. As illustrated in Figure 5, an ion gate is pulsed multiple times (Figure 5b and 5d) in order to isolate multiple precursor ions generated in the same laser shot. Following fragmentation, the ions are reaccelerated (Figure 5d and 5f) into the TOF-2 region of the instrument. The resulting spectrum contains both fragment and precursors for both analyte and standard (Figure 5g) allowing for normalization of signals from the same laser shot. Quantification is performed by on-tissue spotting of a dilution series of standard to generate a calibration curve. This multiplexed approach has been validated by quantifying rifampicin (m/z 821) with a rifapentine standard (m/z 876) in human plasma, and a rabbit liver model. The RSD of rifampicin was 5.1% in a spotted human plasma experiment, a 4-fold improvement in comparison with conventional MALDI MS/MS. A more conservative decrease from 24.9% RSD without normalization to 15.2% with normalization to the standard was observed in a rabbit liver QMSI experiment. Accuracy was also improved, with an increased linear squares correlation coefficient and an average error (calculated by $1/x^2$ weighted linear regression) decrease from 14.4% to 8.2% for spotted human plasma after normalization to the standard, and a marked decrease from 48.3% to 6.3% average relative error ($1/x^0$) in the MSI experiment. MSI quantification of the rabbit liver model agreed with only a 10.6% difference to HPLC-MS/MS results.

3.1.5 Advanced data processing

Improved data analysis approaches also have been explored to reduce signal variability in MSI (62). It has been demonstrated that Poisson statistics more accurately describes the signal and noise variability in MALDI than the commonly assumed Gaussian statistics. The authors compared quantification results obtained using ratios of individual peaks in MALDI spectra to the results obtained using linear Poisson independent component analysis. In this analysis, each component represents a correlated set of peaks with peak intensities described by Poisson statistics. Using this approach, a 2-fold increase in RSD was obtained for multiple samples including milk and extracts of lamb brain and liver tissues in comparison with a traditional peak ratio analysis. The authors indicate that single peak ratios may not be appropriate for quantification in MALDI experiments.

3.2 Ambient Liquid Extraction-Based Techniques

In liquid extraction-based techniques including LMJ-SSP, nano-DESI, LESA, and single probe, molecules are extracted from a specific location on a tissue into a solvent and subsequently ionized by ESI or nanoESI.

3.2.1 Online addition of standards

For quantification, standards are added to the extraction solvent and analyzed together with the extracted analyte mixture. Relative quantification is performed by normalizing the signal of the extracted analyte of interest to the signal of the standard. Meanwhile, absolute quantification requires an additional step, in which the extraction efficiency from different parts of the tissue is determined. It has been demonstrated that a complete extraction is generally not achieved on the time scale of the sampling process. For example, Lanekoff et al. reported ~9% extraction efficiency of nicotine in nano-DESI MSI of dosed rat brain tissue indicating that nicotine was extracted from the top 1 micron layer of the tissue section (38). Meanwhile, Kertesz et al. demonstrated that the extraction efficiency of propanolol using LMJ-SSP in brain, kidney and liver tissues of 10 μm

thickness was in the range of 45-63% (63). The extraction efficiency likely depends on the type and thickness of the tissue section, properties of the analyte and extraction solvent, and scan rate and spatial resolution of the MSI experiment. If the extraction efficiency is known, absolute quantification is straightforward. This approach has been used both for targeted quantification of drugs and metabolites (38) using deuterated standards, and for a shotgun-like quantification of lipids (64) using only one or two standards per lipid class. QMSI of small neurotransmitters in rat brain tissue using nano-DESI showed good reproducibility but fairly large standard deviations attributed to both technical and biological variations between different tissue sections (39).

A modified approach has been developed for quantitative nano-DESI imaging of prostaglandins (PG), important signaling molecules present at low concentrations in tissue samples and difficult to ionize using traditional approaches (48). In this approach, acetonitrile containing 10 ppm of Ag^+ was used as the extraction solvent. Ag^+ ions interact with double bonds thereby improving the ionization of unsaturated molecules like PGs. Complexation with Ag^+ resulted in a 30-fold increase of PG signals. QMSI experiments of mouse uterine tissue sections were performed by adding a deuterated PG standard to the extraction solvent and normalizing the signals of endogenous PGs to the signals of the standard. Quantitative nano-DESI ion images revealed the preferred localization of PG species to both the luminal and glandular epithelium (LE and GE) in the uterine tissue and provided for the first time the distribution of PG concentrations across the sample. PGE_2 was the most abundant species among the five PGs detected reaching concentrations of ~320 nM in LE.

Absolute quantification using direct liquid-extraction based techniques is mainly hindered by difficulties in quantifying the extraction efficiency across different regions of the tissue. An almost complete extraction may be achieved either by placing a probe onto a sample for an extended

period of time (66) or by excising tissue punches (63, 67) for subsequent off-line solvent extraction. Such spatially resolved sampling of tissues is assisted by either LC-MS or LC-MS/MS analysis. Wu et al. used this approach for quantitative spatial profiling of sphingolipids in rat brain tissue by coupling LMJ-SSP to LC-MS (68). The extraction efficiency of ~80% was achieved by adding 1,1,1,3,3,3,-hexafluoro-2-propanol (HFIP) to methanol. An exhaustive surface sampling was carried out by placing the LMJ-SSP probe on the tissue for 2 min followed by 14 min of LC-MS analysis. Spot-by-spot quantification was achieved by adding the appropriate lipid standards to the extraction solvent. Quantitative ion images of sphingolipids in rat brain were validated using bulk extraction LC-MS. The calculated concentrations of different cerebroside species were in the range of 3-45 $\mu g/mm^3$ in the fiber tracts region and 1-30 $\mu g/mm^3$ in the mid-brain region. Despite the accuracy and molecular coverage obtained using this approach, improvements to the spatial resolution and throughput are still needed to make it more compatible with the demands of MSI experiments.

3.2.2 Standards deposited on tissue or prepared with a tissue homogenate

The mimetic tissue model has been used to quantify concentrations of drugs in LESA and DESI MSI (65). LESA was used to create an external calibration curve from liver mimetics spiked with varying concentrations of olanzapine, moxifloxacin, erlotinib and terfenadine. Quantification of these drugs in dosed rat liver tissue section using LESA MSI and DESI MSI produced comparable results. Specifically, concentrations of olanzapine, moxifloxacin, erlotinib and terfenadine at 2 hours post-dose in LESA MSI were 9.3, 15.6, 38.4 and 11.9 nmol/g, respectively and 14.4, 10.8, 26.9 and 12.0 nmol/g, respectively in DESI MSI.

Quantification of analytes deposited onto a sample has been used to examine the validity of QMSI experiments performed using spray-based techniques including DESI and its analogs.

Homogenous deposition of the analyte is key to the accurate quantification and may be achieved using micropippeting, spraying, and ink-jet printing (69).

Chemical reagents also have been deposited onto the tissue for selective derivatization of targeted molecules. This on-tissue derivatization approach was used by Shariatgorji et al. to improve the sensitivity of detection of neurotransmitters and neuroactive drugs containing primary amino groups via their reaction with pyrylium salts (70). Quantitative DESI-MSI was performed for the fluvoxamine drug in brain tissue sections. In this experiment, deuterated fluvoxamine (d4-fluvoxamine) was deposited onto the tissue along with pyrylium salt 2,4-diphenyl-pyranylium tetrafluoroborate reagent (DPP-TFB). Due to the presence of the derivatizing agent, both the drug and the standard undergo conversion to their corresponding pyridinium cation. Aliquots of 0.2 µL of fluvoxamine at different concentrations ranging from 0.02 mg/mL to 0.032 µg/mL using a dilution factor of 5 were spotted on control tissue sections as shown in **Figure 6a.** A calibration curve was constructed by plotting the derivatized fluvoxamine/d4-fluvoxamine ratio against the amount of fluvoxamine spotted onto the tissue section (**Figure 6b**). Fluvoxamine dosed tissue sections are observed in **Figure 6c** showing preferred localization in the ventral striatum, thalamus and cerebellum. **Figure 6d** shows the quantification of dosed fluvoxamine in different parts of the brain using the average spectrum in every specific structure. The highest concentration of fluvoxamine of ~100 pmol/mg of tissue was found in the ventral striatum region of the brain.

An interesting strategy recently reported in the literature, introduces the concept of "virtual calibration" to account for regional matrix effects without the use of synthetic standards (71). In this approach, region-specific endogenous metabolites strongly correlated to the ion intensity changes of the analyte are selected as "native internal standards" and used to assess matrix effects. A machine-learning regression model is used to fit the relationship between the signal intensities

of the standards and the signal intensity of the analyte in different types of tissue. This training model is applied to predict a relative calibration factor (f_r), which is used to correct the signal of the analyte (I_{pix}) in every pixel. For quantification, an external calibration curve is constructed using a mimetic tissue that correlates the calibrated signal of the analyte (I_{pix}/f_r) to its concentration. Using this approach and liver mimetic sections for calibration, the concentration of an LXY drug candidate over a whole body section was quantified. Ten endogenous metabolites were selected as standards. Comparison of the calibration factors obtained from different organs revealed that matrix effects are more dominant in the heart and lung tissues. Matrix effects were effectively accounted for using virtual calibration and the concentration of the drug was quantified in every organ. It was found that the drug preferably accumulated in the heart reaching a concentration of 3 pmol/mm^2, which is in a good agreement with the concentration of 4 pmol/mm^2 calculated using the TEC approach. Although this study was carried out using a spray-based technique, it can be readily extended to laser -or plasma-based techniques.

4. PROTEIN IMAGING

4.1 Quantitative Imaging of Intact Proteins

Soft ionization techniques have been traditionally used for imaging of intact proteins (72–74). Most of the studies in this field employed MALDI MSI and were focused on the spatial localization of the proteins rather than quantification. Quantification of intact proteins observed in MSI experiments is challenging due to the uncertainty in the ionization efficiency and signal suppression in different parts of the tissue. Recently, the mimetic tissue model has been used for the quantification of ubiquitin in MSI experiments performed using LESA (75). Specifically, a homogenized rat brain tissue spiked with ^{13}C, ^{15}N-labeled ubiquitin was used as a mimetic model. The mimetic tissue model material was sectioned and analyzed alongside rat brain tissue sections. A calibration plot obtained at different concentrations of the isotopically labeled ubiquitin in the mimetic tissue sample provided the upper limit of quantification of 163 nmol/g tissue. The average concentration of ubiquitin across the rat brain tissue was around 130 nmol/g, which is consistent with the LC/MS data. This study established an approach for the targeted quantification of proteins in tissue sections in LESA-MSI experiments, which can be readily extended to other sampling/ionization techniques.

Protein identification is one of the biggest challenges in MSI experiments. One experimental strategy designed to address this challenge involves on-tissue enzymatic digestion followed by imaging of the resulting peptides (73). The development of nanoPOTS (Nanodroplet Processing in One pot for Trace Samples) (76), a highly sensitive platform that enables a complete proteomics workflow to be performed in a ~200 nanoliter volume of solvent, has opened up unique opportunities for both imaging and identification of thousands of proteins in tissue sections with a

spatial resolution of better than 100 μm (77). In this experiment, tissue voxels are generated using laser capture microdissection and capture of the excised tissue into individual nanowells on a specially designed chip. An automated proteomics workflow performed in the nanowells includes protein extraction and denaturation, protein alkylation, digestion, and transfer to a 96-well plate for subsequent analysis by LC-MS/MS. A log transformation of the relative peptide abundances followed by normalization and rollup from scaled peptide abundances to the protein level yields normalized relative protein abundances. This approach enables relative quantification by comparison of the abundance of the same protein in different voxels. NanoPOTS was employed to obtain >2000 protein images in mouse uterine tissues on day 4 of pregnancy. The results were validated against bulk analysis of the different cell types present in the tissue. This study provided a detailed proteomics map for the distinct cell types present in the tissue. It demonstrated how protein localization is linked to important biochemical processes in this system. For example, proteins related to remodeling of the extracellular matrix in preparation to embryo implantation were found to be enhanced in stroma. Meanwhile, proteins related to epithelial cell crypt formation were found to be localized to luminal epithelium.

4.2 Quantitative Elemental Imaging of Metals and Proteins in Biological Samples

Inductively coupled plasma mass spectrometry (ICP-MS) is an established technique for the quantitative elemental analysis of complex samples (78). Under typical ICP conditions, analyte molecules are completely dissociated into their atomic constituents and small polyatomic ions, which are subsequently analyzed using mass spectrometry. Accurate quantification is made possible due to the fact that the ionization efficiency is compound-independent and, therefore, ion abundances are directly correlated to the elemental composition and concentration of each

compound (79). Coupling of laser ablation (LA) with ICP-MS (LA-ICP-MS) (80, 81), enabled spatial elemental profiling of biological samples (82, 83). The technique offers below parts-per-million detection limits, up to nine orders of magnitude dynamic range, down to 1 micron spatial resolution.

By combining LA-ICP-MS with immunohistochemical staining using lanthanide-labeled antibodies, Giesen et al. have extended the capabilities of this technique to the targeted imaging of proteins in tissues (84). In that study, three tumor markers (MUC 1, Her 2, and CK 7) were detected in formalin-fixed paraffin embedded tissues of human breast cancer. Although signal intensities in LA-ICP-MS experiments increase with tissue thickness, the authors reported that best-quality results were obtained using 5 μm- thick sections, which are less likely to crack during laser ablation. Other important conditions include laser energy, spot size, and scan rate along with antibody concentration and incubation time.

In both the elemental and protein imaging by LA-ICP-MS, quantification typically relies on matrix-matched standards, which are not always available (85). In an ideal LA experiment, all the elements are removed from the sample and transported to the ICP-MS with the same efficiency. One of key issues is elemental fractionation, which is affected by the physical properties and chemical composition of the sample along with laser wavelength, pulse duration, energy, and repetition rate. It has been demonstrated that fractionation is less pronounced in experiments utilizing femtosecond lasers, which generate high-quality craters and more monodisperse particles in the ablation process.

The experimental factors affecting quantification in LA-ICP-MS include fluctuations in laser power output, variations in transport efficiency and amount of ablated material, and signal instability. Selection of appropriate standards for LA-ICP-MS experiments is challenging and

usually limited to elements present in the sample matrix; standard should be present in the sample at a known concentration. For tissue samples, ^{13}C is typically used for quantification. Typical %RSD obtained in these experiments is below 10%. However, the assumption that carbon concentration is constant across a tissue section is difficult to justify and there is experimental evidence that variations in the chemical composition of carbon-rich matrices may affect the accuracy of both ^{12}C- and ^{13}C-based normalization strategies. Furthermore, differences in the partitioning of carbon and other elements within the particle phase and into the vapor phase in the ablation plume demonstrated for polymer samples must be quantified for biological samples to verify the robustness of carbon isotopes as standards (86).

Other normalization approaches rely on the measurement of the ablated mass using acoustic or optical techniques. It is assumed that similar particle distributions are generated in the ablation of different samples and that signal response in ICP-MS is only dependent on the ablated mass. Both assumptions ignore processes occurring in the ablation plume and, therefore, such mass normalization approaches have limited utility.

Sample preparation can introduce experimental artifacts and, therefore, has been extensively investigated and validated to ensure accurate quantification. Metal concentrations are affected by the extent to which metals are either added or removed from the sample in the sample preparation and storage steps. Leaching of the metals during tissue embedding, freezing, and long-term storage has been reported. Snap freezing in liquid nitrogen reduces metal loss during sample preparation but does not completely rule it out. Sample contamination during sectioning can be minimized using metal-free blades and clean glass slides.

Although no common calibration method works for all types of biological samples, a majority of quantification approaches in LA-ICP-MS utilize matrix-matched standards, which

effectively compensate for both fractionation and matrix effects. Matrix effect in ICP-MS are most pronounced for heavy elements with low ionization potentials and increase with increase in concentration. Ideally, certified reference materials (CRMs) are used in these experiments. However, only a limited number of CRMs is available to biological tissue imaging experiments. As a result, substantial effort has been dedicated to the development of custom laboratory prepared standards including tissue homogenate spiked with standards containing appropriate elements. Several procedures have been developed to ensure good control of the water content and homogeneity of the standard samples necessary for accurate quantification. However, it is difficult to assess the extent of the mismatch between the water content in the standard and sample, which may affect the results of quantification.

Thin polymer films and films of spiked agarose gel have been examined as an alternative to matrix-matched tissue standards. Such films could enable the implementation of isotope dilution mass spectrometry techniques to LA-ICP-MS imaging experiments. Gelatin thin films spiked with metal standards have been used for imaging of cerium oxide nanoparticles in different tissues providing insights into the origin of its toxicity (87). Matrix-matched gelatin standards also have been used to support quantitative super resolution imaging using LA-ICP-MS (88).

Another innovative strategy involving labeling with antibodies conjugated with gold nanoclusters (AuNC) has been introduced to enable highly sensitive protein detection and accurate quantification (89). In this approach, an antibody is labeled with AuNCs using carbodiimide cross linking and the resulting bioconjugate is used for tissue staining as illustrated in **Figure 7**. The stoichiometry of the bioconjugate was confirmed to be 1:1 and the size of an individual AuNC was 2.7±0.1 nm corresponding to an average of 579 gold atoms per bioconjugate. This labeling approach results in a substantial increase in the Au^+ signal in ICP-MS, which is referred to as

signal amplification. Gelatin matrix-matched internal standards are prepared using established approaches and analyzed in parallel with the stained tissue sections. The approach was used for quantitative imaging of metallothioneins in human retina tissue sections. Calibration curves were obtained for two different standards (AuNCs and $NaAuCl_4 \bullet H_2O$), which showed similar sensitivity indicating that gelatin films spiked with $NaAuCl_4$ are appropriate standards for quantification. The observed localization of metallothioneins in retina tissues was consistent with literature results and the average concentrations were consistent with the results obtained for tissue homogenates using ELISA.

Similar approach was used to measure iron and ferroportin in the hippocampus region of brain tissues of Alzheimer's disease patients (90). The same tissues were analyzed using fluorescence microscopy and LA-ICP-MS. Ferroportin expression was also evaluated using conventional immunohistochemistry. Because the uncertainty in the diameter of AuNCs contributes to the uncertainty in protein quantification, the authors synthesized more homogeneous 2.20 ± 0.04 nm AuNCs containing on average 314 gold atoms. In contrast with traditional methods, the immunohistochemistry-based LA-ICP-MS enables imaging of both total and protein-bound iron. Other strategies for absolute protein quantification using ICP-MS are summarized in a recent review (91).

5. CONCLUSIONS AND OUTLOOK

QMSI experiments present challenges and opportunities. Accurate quantification achieved using LA-ICP-MS techniques has been extensively validated. Meanwhile, QMSI using soft ionization techniques is still in early stages of development and detailed assessment of the accuracy and reproducibility of the existing approaches must be performed. Matrix effects present a major

challenge for quantifying the ionization efficiency in QMSI experiments and must be accounted for to enable accurate quantification. Furthermore, the extraction efficiency of analytes must be further improved and quantified. Despite these challenges, QMSI based on soft ionization techniques has already provided important insights into the localization and abundance of small metabolites and lipids in tissue sections. Several innovative approaches have been developed to enable either targeted or untargeted quantification of proteins in MSI experiments. Further improvements in the spatial resolution and throughput of nanoPOTS and related techniques will open new directions in untargeted spatially-resolved proteomics.

New approaches for QMSI are emerging to expand the range of compounds amenable to quantification and improve the accuracy of these experiments. For example, photo-cleavable probes have been used for the quantification of glycans, which are difficult to detect in MSI experiments due to their low ionization efficiency and signal suppression (92). The probes were designed to selectively target amino groups and contained chromophores, which could be cleaved using a 355 nm laser. Using four different probes, four types of glycans in single cells and tissues could be observed. Matrix-free laser desorption ionization techniques show promise for broadening the molecular coverage in laser-based QMSI experiments (93, 94). Similarly, the parameter space of solvent dopants used in liquid extraction based QMSI techniques has not been fully explored.

New online derivatization approaches along with optimization of the extraction solvent composition for a specific system will enable imaging of low ionization efficiency species in tissue samples. Coupling of MSI with ion mobility separation has been used to both improve molecular coverage and facilitate identification of biomolecules in tissue samples (95–97). Implementation of QMSI in combination with ion mobility separation is a natural next step in the development of

this promising technique. Finally, validated approaches that facilitate simultaneous quantification of multiple classes of compounds will increase the experimental throughput.

6. ACKNOWLEDGEMENTS

The authors acknowledge support from the National Science Foundation (NSF-1808136, JL) and the National Institutes of Health (NIH) Common Fund, through the Office of Strategic Coordination/Office of the NIH Director under award UG3HL145593 (HuBMAP Program, JL). DMS acknowledges support from the National Science Foundation Graduate Research Fellowship under Grant No. (DGE-1333468). Any opinions, findings, and conclusions or recommendations expressed in this material are those of the authors and do not necessarily reflect the views of the NSF or NIH.

7. LITERATURE CITED

1. Fenn JB, Mann M, Meng CK, Wong SF, Whitehouse CM. 1990. Electrospray ionization–principles and practice. *Mass Spectrom. Rev.* 9(1):37–70
2. Hillenkamp F, Karas M, Beavis RC, Chait BT. 1991. Matrix-assisted laser desorption/ionization mass spectrometry of biopolymers. *Anal. Chem.* 63(24):1193A–1203A
3. Norris JL, Caprioli RM. 2013. Analysis of tissue specimens by matrix-assisted laser desorption/ionization imaging mass spectrometry in biological and clinical research. *Chem. Rev.* 113(4):2309–42
4. Wu C, Dill AL, Eberlin LS, Cooks RG, Ifa DR. 2013. Mass spectrometry imaging under ambient conditions. *Mass Spectrom. Rev.* 32(3):218–43
5. Watrous JD, Dorrestein PC. 2011. Imaging mass spectrometry in microbiology. *Nat. Rev. Microbiol.* 9(9):683–94
6. Swales JG, Hamm G, Clench MR, Goodwin RJA. 2019. Mass spectrometry imaging and its application in pharmaceutical research and development: a concise review. *Int. J. Mass Spectrom.* 437:99–112
7. Buchberger AR, DeLaney K, Johnson J, Li L. 2018. Mass spectrometry imaging: a review of emerging advancements and future insights. *Anal. Chem.* 90(1):240–65
8. Rubakhin SS, Jurchen JC, Monroe EB, Sweedler J V. 2005. Imaging mass spectrometry: fundamentals and applications to drug discovery. *Drug Discov. Today*. 10(12):823–37
9. McDonnell LA, Heeren RMA. 2007. Imaging mass spectrometry. *Mass Spectrom. Rev.* 26(4):606–43
10. Trufelli H, Palma P, Famiglini G, Cappiello A. 2011. An overview of matrix effects in liquid chromatography-mass spectrometry. *Mass Spectrom. Rev.* 30(3):491–509
11. Taylor PJ. 2005. Matrix effects: The Achilles heel of quantitative high-performance liquid chromatography-electrospray-tandem mass spectrometry. *Clin. Biochem.* 38(4):328–34
12. Nagana Gowda GA, Djukovic D. 2014. Overview of mass spectrometry-based metabolomics: opportunities and challenges. *Methods Mol. Biol.* 1198:3–12
13. Lei Z, Huhman D V., Sumner LW. 2011. Mass spectrometry strategies in metabolomics. *J. Biol. Chem.* 286(29):25435–42
14. Khoury S, Canlet C, Lacroix MZ, Berdeaux O, Jouhet J, Bertrand-Michel J. 2018. Quantification of lipids: model, reality, and compromise. *Biomolecules*. 8(4):174
15. Koivusalo M, Haimi P, Heikinheimo L, Kostiainen R, Somerharju P. 2001. Quantitative determination of phospholipid compositions by ESI-MS: effects of acyl chain length, unsaturation, and lipid concentration on instrument response. *J. Lipid Res.* 42:663–72
16. Bantscheff M, Schirle M, Sweetman G, Rick J, Kuster B. 2007. Quantitative mass spectrometry in proteomics: a critical review. *Anal. Bioanal. Chem.* 389:1017–31
17. Ong SE, Mann M. 2005. Mass spectrometry–based proteomics turns quantitative. *Nat. Chem. Biol.* 1:252–62

18. Caprioli RM, Farmer TB, Gile J. 1997. Molecular imaging of biological samples: localization of peptides and proteins using MALDI-TOF MS. *Anal. Chem.* 69(23):4751–60

19. Cornett DS, Reyzer ML, Chaurand P, Caprioli RM. 2007. MALDI imaging mass spectrometry: molecular snapshots of biochemical systems. *Nat. Methods*. 4:828–33

20. Walch A, Rauser S, Deininger SO, Höfler H. 2008. MALDI imaging mass spectrometry for direct tissue analysis: a new frontier for molecular histology. *Histochem. Cell Biol.* 130(3):421–34

21. Chen H, Gamez G, Zenobi R. 2009. What can we learn from ambient ionization techniques? *J. Am. Soc. Mass Spectrom.* 20(11):1947–63

22. Laskin J, Lanekoff I. 2016. Ambient mass spectrometry imaging using direct liquid extraction techniques. *Anal. Chem.* 88(1):52–73

23. Ifa DR, Wu C, Ouyang Z, Cooks RG. 2010. Desorption electrospray ionization and other ambient ionization methods: current progress and preview. *Analyst*. 135(4):669–81

24. Venter AR, Douglass KA, Shelley JT, Hasman G, Honarvar E. 2014. Mechanisms of real-time, proximal sample processing during ambient ionization mass spectrometry. *Anal. Chem.* 86(1):233–49

25. Nemes P, Vertes A. 2007. Laser ablation electrospray ionization for atmospheric pressure, in vivo, and imaging mass spectrometry. *Anal. Chem.* 79(21):8098–8106

26. Sampson JS, Hawkridge AM, Muddiman DC. 2006. Generation and detection of multiply-charged peptides and proteins by matrix-assisted laser desorption electrospray ionization (MALDESI) fourier transform ion cyclotron resonance mass spectrometry. *J. Am. Soc. Mass Spectrom.* 17(12):1712–16

27. Takáts Z, Wiseman JM, Gologan B, Cooks RG. 2004. Mass spectrometry sampling under ambient conditions with desorption electrospray ionization. *Science.* 306(5695):471–73

28. Wiseman JM, Ifa DR, Zhu Y, Kissinger CB, Manicke NE, et al. 2008. Desorption electrospray ionization mass spectrometry: imaging drugs and metabolites in tissues. *Proc. Natl. Acad. Sci. U. S. A.* 105(47):18120–25

29. Roach PJ, Laskin J, Laskin A. 2010. Nanospray desorption electrospray ionization: An ambient method for liquid-extraction surface sampling in mass spectrometry. *Analyst*. 135:2233–36

30. Van Berkel GJ, Sanchez AD, Martin Quirke JE. 1992. Thin Layer Chromatography Coupled to Mass Spectrometry. In Handbook of Thin Layer Chromatography; Sherma. *Fresenius J. Anal. Chem*. 856(1):6216–23

31. Kertesz V, Van Berkel GJ. 2010. Fully automated liquid extraction-based surface sampling and ionization using a chip-based robotic nanoelectrospray platform. *J. Mass Spectrom.* 45(3):252–60

32. Lietz CB, Gemperline E, Li L. 2013. Qualitative and quantitative mass spectrometry imaging of drugs and metabolites. *Adv. Drug Deliv. Rev.* 65(8):1074–85

33. Lanekoff I, Laskin J. 2018. Quantitative mass spectrometry imaging of molecules in

biological systems. In *Advances in Chromatography*, ed E Grushka, N Grinberg. 54:43–72. Boca Raton: CRC Press

34. Porta T, Lesur A, Varesio E, Hopfgartner G. 2015. Quantification in MALDI-MS imaging: what can we learn from MALDI-selected reaction monitoring and what can we expect for imaging? *Anal. Bioanal. Chem.* 407(8):2177–87

35. Ellis SR, Bruinen AL, Heeren RMA. 2014. A critical evaluation of the current state-of-the-art in quantitative imaging mass spectrometry. *Anal. Bioanal. Chem.* 406(5):1275–89

36. Lanekoff I, Stevens SL, Stenzel-Poore MP, Laskin J. 2014. Matrix effects in biological mass spectrometry imaging: identification and compensation. *Analyst*. 139(14):3528–32

37. Rohner TC, Staab D, Stoeckli M. 2005. MALDI mass spectrometric imaging of biological tissue sections. *Mech. Ageing Dev.* 126(1):177–85

38. Lanekoff I, Thomas M, Carson JP, Smith JN, Timchalk C, Laskin J. 2013. Imaging nicotine in rat brain tissue by use of nanospray desorption electrospray ionization mass spectrometry. *Anal. Chem.* 85(2):882–89

39. Bergman HM, Lundin E, Andersson M, Lanekoff I. 2016. Quantitative mass spectrometry imaging of small-molecule neurotransmitters in rat brain tissue sections using nanospray desorption electrospray ionization. *Analyst*. 141(12):3686–95

40. Taylor AJ, Dexter A, Bunch J. 2018. Exploring ion suppression in mass spectrometry imaging of a heterogeneous tissue. *Anal. Chem.* 90(9):5637–45

41. Perry WJ, Patterson NH, Prentice BM, Neumann EK, Caprioli RM, Spraggins JM. 2019. Uncovering matrix effects on lipid analyses in MALDI imaging mass spectrometry experiments. *J. Mass Spectrom.* 55(4):e4491

42. Yang C, Lee HK, Zhang Y, Jiang LL, Chen ZF, et al. 2019. In situ detection and imaging of PFOS in mouse kidney by matrix-assisted laser desorption/ionization imaging mass spectrometry. *Anal. Chem.* 91(14):8783–88

43. Rzagalinski I, Kovačević B, Hainz N, Meier C, Tschernig T, Volmer DA. 2018. Toward higher sensitivity in quantitative MALDI imaging mass spectrometry of CNS drugs using a nonpolar matrix. *Anal. Chem.* 90(21):12592–600

44. Sugiyama E, Masaki N, Matsushita S, Setou M. 2015. Ammonium sulfate improves detection of hydrophilic quaternary ammonium compounds through decreased ion suppression in matrix-assisted laser desorption/ionization imaging mass spectrometry. *Anal. Chem.* 87(22):11176–81

45. Barré FPY, Flinders B, Garcia JP, Jansen I, Huizing LRS, et al. 2016. Derivatization strategies for the detection of triamcinolone acetonide in cartilage by using matrix-assisted laser desorption/ionization mass spectrometry imaging. *Anal. Chem.* 88(24):12051–59

46. Unsihuay D, Qiu J, Swaroop S, Nagornov KO, Kozhinov AN, et al. 2020. Imaging of triglycerides in tissues using nanospray desorption electrospray ionization (nano-DESI) mass spectrometry. *Int. J. Mass Spectrom.* 448:116269

47. Eberlin LS, Ferreira CR, Dill AL, Ifa DR, Cheng L, Cooks RG. 2011. Nondestructive, histologically compatible tissue imaging by desorption electrospray ionization mass

spectrometry. *ChemBioChem*. 12(14):2129–32

48. Duncan KD, Fang R, Yuan J, Chu RK, Dey SK, et al. 2018. Quantitative mass spectrometry imaging of prostaglandins as silver ion adducts with nanospray desorption electrospray ionization. *Anal. Chem.* 90(12):7246–7252

49. Lostun D, Perez CJ, Licence P, Barrett DA, Ifa DR. 2015. Reactive DESI-MS imaging of biological tissues with dicationic ion-pairing compounds. *Anal. Chem.* 87(6):3286–93

50. Wu C, Ifa DR, Manicke NE, Cooks RG. 2009. Rapid, direct analysis of cholesterol by charge labeling in reactive desorption electrospray ionization. *Anal. Chem.* 81(18):7618–24

51. Rzagalinski I, Volmer DA. 2017. Quantification of low molecular weight compounds by MALDI imaging mass spectrometry – a tutorial review

52. Chumbley CW, Reyzer ML, Allen JL, Marriner GA, Via LE, et al. 2016. Absolute quantitative MALDI imaging mass spectrometry: a case of rifampicin in liver tissues. *Anal. Chem.* 88(4):2392–98

53. Hansen HT, Janfelt C. 2016. Aspects of quantitation in mass spectrometry imaging investigated on cryo-sections of spiked tissue homogenates. *Anal. Chem.* 88(23):11513–20

54. Barry JA, Groseclose MR, Castellino S. 2019. Quantification and assessment of detection capability in imaging mass spectrometry using a revised mimetic tissue model. *Bioanalysis*. 11(11):1099–1116

55. Song X, He J, Li C, Sun C, Pang X, et al. 2019. Fabrication of homogenous three-dimensional biomimetic tissue for mass spectrometry imaging. *J. Mass Spectrom.* 54(5):378–88

56. Giordano S, Morosi L, Veglianese P, Licandro SA, Frapolli R, et al. 2016. 3D mass spectrometry imaging reveals a very heterogeneous drug distribution in tumors. *Sci. Rep.* 6:37027

57. Nazari M, Bokhart MT, Loziuk PL, Muddiman DC. 2018. Quantitative mass spectrometry imaging of glutathione in healthy and cancerous hen ovarian tissue sections by infrared matrix-assisted laser desorption electrospray ionization (IR-MALDESI). *Analyst*. 143:654

58. Grey AC, Demarais NJ, West BJ, Donaldson PJ. 2019. A quantitative map of glutathione in the aging human lens. *Int. J. Mass Spectrom.* 437:58–68

59. Barry JA, Ait-Belkacem R, Hardesty WM, Benakli L, Andonian C, et al. 2019. Multicenter validation study of quantitative imaging mass spectrometry. *Anal. Chem.* 91(9):6266–74

60. Prentice BM, Chumbley CW, Hachey BC, Norris JL, Caprioli RM. 2016. Multiple time-of-flight/time-of-flight events in a single laser shot for improved matrix-assisted laser desorption/ionization tandem mass spectrometry quantification. *Anal. Chem.* 88(19):9780–88

61. Prentice BM, Chumbley CW, Caprioli RM. 2017. Absolute quantification of rifampicin by MALDI imaging mass spectrometry using multiple TOF/TOF events in a single laser shot. *J. Am. Soc. Mass Spectrom.* 28(1):136–44

62. Deepaisarn S, Tar PD, Thacker NA, Seepujak A, McMahon AW. 2018. Quantifying biological samples using linear poisson independent component analysis for MALDI-ToF mass spectra. *Bioinformatics*. 34(6):1001–8

63. Kertesz V, Weiskittel TM, Vavrek M, Freddo C, Van Berkel GJ. 2016. Extraction efficiency and implications for absolute quantitation of propranolol in mouse brain, liver and kidney tissue sections using droplet-based liquid microjunction surface sampling high-performance liquid chromatography/electrospray ionization tande. *Rapid Commun. Mass Spectrom.* 30(14):1705–12

64. Lanekoff I, Thomas M, Laskin J. 2014. Shotgun approach for quantitative imaging of phospholipids using nanospray desorption electrospray ionization mass spectrometry. *Anal. Chem.* 86(3):1872–80

65. Swales JG, Strittmatter N, Tucker JW, Clench MR, Webborn PJH, Goodwin RJA. 2016. Spatial quantitation of drugs in tissues using liquid extraction surface analysis mass spectrometry imaging. *Sci. Rep.* 6:37648

66. Chen X, Hatsis P, Judge J, Argikar UA, Ren X, et al. 2016. Compound property optimization in drug discovery using quantitative surface sampling micro liquid chromatography with tandem mass spectrometry. *Anal. Chem.* 88(23):11813–20

67. Cahill JF, Kertesz V, Weiskittel TM, Vavrek M, Freddo C, Van Berkel GJ. 2016. Online, absolute quantitation of propranolol from spatially distinct 20- and 40-µm dissections of brain, liver, and kidney thin tissue sections by laser microdissection-liquid vortex capture-mass spectrometry. *Anal. Chem.* 88(11):6026–34

68. Wu Q, Huang Z, Wang Y, Zhang Z, Lu H. 2020. Absolute quantitative imaging of sphingolipids in brain tissue by exhaustive liquid microjunction surface sampling–liquid chromatography–mass spectrometry. *J. Chromatogr. A*. 1609:460436

69. Luo Z, He J, He J, Huang L, Song X, et al. 2018. Quantitative analysis of drug distribution by ambient mass spectrometry imaging method with signal extinction normalization strategy and inkjet-printing technology. *Talanta*. 179:230–37

70. Shariatgorji M, Strittmatter N, Nilsson A, Källback P, Alvarsson A, et al. 2016. Simultaneous imaging of multiple neurotransmitters and neuroactive substances in the brain by desorption electrospray ionization mass spectrometry. *Neuroimage*. 136:129–38

71. Song X, He J, Pang X, Zhang J, Sun C, et al. 2019. Virtual calibration quantitative mass spectrometry imaging for accurately mapping analytes across heterogenous biotissue. *Anal. Chem.* 91(4):2838–2846

72. Stoeckli M, Chaurand P, Hallahan DE, Caprioli RM. 2001. Imaging mass spectrometry: a new technology for the analysis of protein expression in mammalian tissues. *Nat. Med.* 7:493–96

73. Groseclose MR, Andersson M, Hardesty WM, Caprioli RM. 2007. Identification of proteins directly from tissue: in situ tryptic digestions coupled with imaging mass spectrometry. *J. Mass Spectrom.* 42(2):254–62

74. Crecelius A, Caprioli R, Williams B, Dawant B, Bodenheimer B. 2005. Three-dimensional visualization of protein expression in mouse brain structures using imaging

mass spectrometry. *J. Am. Soc. Mass Spectrom.* 16(7):1093–99

75. Havlikova J, Randall EC, Griffiths RL, Swales JG, Goodwin RJA, et al. 2019. Quantitative imaging of proteins in tissue by stable isotope labeled mimetic liquid extraction surface analysis mass spectrometry. *Anal. Chem.* 91(22):14198–202

76. Zhu Y, Dou M, Piehowski PD, Liang Y, Wang F, et al. 2018. Spatially resolved proteome mapping of laser capture microdissected tissue with automated sample transfer to nanodroplets. *Mol. Cell. Proteomics*. 17(9):1864–74

77. Piehowski PD, Zhu Y, Bramer LM, Stratton KG, Zhao R, et al. 2020. Automated mass spectrometry imaging of over 2000 proteins from tissue sections at 100-μm spatial resolution. *Nat. Commun.* 11(1):8

78. Beauchemin D. 2008. Inductively coupled plasma mass spectrometry. *Anal. Chem.* 80(12):4455–86

79. Hare D, Austin C, Doble P. 2012. Quantification strategies for elemental imaging of biological samples using laser ablation-inductively coupled plasma-mass spectrometry. *Analyst*. 137(7):1527–37

80. Durrant SF, Ward NI. 1994. Laser ablation-inductively coupled plasma-mass spectrometry (LA-ICP-MS) for the multielemental analysis of biological materials: a feasibility study. *Food Chem.* 49(3):317–23

81. Gray AL. 1985. Solid sample introduction by laser ablation for inductively coupled plasma source mass spectrometry. *Analyst*. 110(5):551–56

82. Sussulini A, Becker JS, Becker JS. 2017. Laser ablation ICP-MS: application in biomedical research. *Mass Spectrom. Rev.* 36(1):47–57

83. Pozebon D, Scheffler GL, Dressler VL, Nunes MAG. 2014. Review of the applications of laser ablation inductively coupled plasma mass spectrometry (LA-ICP-MS) to the analysis of biological samples. *J. Anal. At. Spectrom.* 29(12):2204–28

84. Giesen C, Mairinger T, Khoury L, Waentig L, Jakubowski N, Panne U. 2011. Multiplexed immunohistochemical detection of tumor markers in breast cancer tissue using laser ablation inductively coupled plasma mass spectrometry. *Anal. Chem.* 83(21):8177–83

85. Hare D, Austin C, Doble P. 2012. Quantification strategies for elemental imaging of biological samples using laser ablation-inductively coupled plasma-mass spectrometry. *Analyst*. 137(7):1527–37

86. Todoli JL, Mermet JM. 1998. Study of polymer ablation products obtained by ultraviolet laser ablation - inductively coupled plasma atomic emission spectrometry. *Spectrochim. acta, Part B At. Spectrosc.* 53(12):1645–56

87. Chen B, Lum JTS, Huang Y, Hu B, Leung KSY. 2019. Integration of sub-organ quantitative imaging LA-ICP-MS and fractionation reveals differences in translocation and transformation of CeO2 and Ce3+ in mice. *Anal. Chim. Acta*. 1082:18–29

88. Westerhausen MT, Bishop DP, Dowd A, Wanagat J, Cole N, Doble PA. 2019. Super-resolution reconstruction for two-and three-dimensional LA-ICP-MS bioimaging. *Anal. Chem.* 91(23):14879–86

89. Cruz-Alonso M, Fernandez B, García M, González-Iglesias H, Pereiro R. 2018. Quantitative imaging of specific proteins in the human retina by laser ablation ICPMS using bioconjugated metal nanoclusters as labels. *Anal. Chem.* 90(20):12145–51

90. Cruz-Alonso M, Fernandez B, Navarro A, Junceda S, Astudillo A, Pereiro R. 2019. Laser ablation ICP-MS for simultaneous quantitative imaging of iron and ferroportin in hippocampus of human brain tissues with Alzheimer's disease. *Talanta*. 197:413–21

91. Cid-Barrio L, Calderón-Celis F, Abásolo-Linares P, Fernández-Sánchez ML, Costa-Fernández JM, et al. 2018. Advances in absolute protein quantification and quantitative protein mapping using ICP-MS. *TrAC - Trends Anal. Chem.* 104:148–59

92. Han J, Huang X, Liu H, Wang J, Xiong C, Nie Z. 2019. Laser cleavable probes for in situ multiplexed glycan detection by single cell mass spectrometry. *Chem. Sci.* 10(47):10958–62

93. Muthu M, Gopal J, Chun S. 2017. Nanopost array laser desorption ionization mass spectrometry (NAPA-LDI MS): gathering moss? *TrAC - Trends Anal. Chem.* 97:96–103

94. Korte AR, Morris NJ, Vertes A. 2019. High throughput complementary analysis and quantitation of metabolites by MALDI- and silicon nanopost array-laser desorption/ionization-mass spectrometry. *Anal. Chem.* 91(6):3951–58

95. Sans M, Feider CL, Eberlin LS. 2018. Advances in mass spectrometry imaging coupled to ion mobility spectrometry for enhanced imaging of biological tissues. *Curr. Opin. Chem. Biol.* 42:138–46

96. Woods AS, Jackson SN. 2010. The application and potential of ion mobility mass spectrometry in imaging MS with a focus on lipids. *Methods Mol. Biol.* 656:99–111

97. Kiss A, Heeren RMA. 2011. Size, weight and position: ion mobility spectrometry and imaging MS combined. *Anal. Bioanal. Chem.* 399:2623–34

8. FIGURE CAPTIONS

Figure 1. An optical image of an MCAO brain tissue section with the ischemic region marked in pink and white matter marked in cyan (*top*). Ion images of $[M + Na]^+$ and $[M + K]^+$ of the PC 43:6 standard and endogenous PC 34:1 and PC 38:4. Ion images normalized to the TIC and PC 25:0 standard are denoted with "Norm TIC" and "Norm Std", respectively. Lateral scale bar is 2 mm. Intensity scale bar ranges from 0 (black) to 100% (light yellow) signal intensity of an individual peak. Figure adapted from Reference 36. Reproduced by permission of The Royal Society of Chemistry

[**Note to Annual Reviews: I am an author of this article; the publisher grants authors the right to reuse their own figures without permission.**]

Figure 2. a) TEC and **b)** normalized TEC values calculated in DESI (left) and MALDI (right) for olanzapine as $[M + H]^+$ adduct (*m/z* 313.14) deposited on 10 µm mouse brain sections. Anatomical regions corresponding to the molecular (Mo) and granular (Gr) layers of the cerebellum, hippocampus (Hipp), and white matter (WM), which were successfully segmented using the graph-cuts clustering, are indicated with different color bars. **c)** Normalized TIC ion images of protonated olanzapine obtained with DESI and MALDI are shown in the left panel whereas normalized ion images of protonated olanzapine by cluster specific TECs are shown in the right panel for 15 clusters. Figure adapted with permission from Reference 40. Copyright (2018) American Chemical Society.

Figure 3. Illustration of the four methods of applying standards for IMS. Depositing the standards on the tissue section requires thaw-mounting the section followed by application of the standards and matrix. Deposition under the tissue section requires spotting the standards first, thaw-mounting the section on top of them, and then applying matrix. A sandwich method combines depositing the standards under and on the tissue section followed by matrix. Premixing the standard involves thaw-mounting the tissue section followed by depositing the standards and the matrix in a single solution. Figure reproduced with permission from Reference 52. Copyright (2016) American Chemical Society.

Figure 4. Schematic outlining the workflow for the generation and application of a mimetic tissue model for QMSI. The process involves spiking tissue homogenates with low volumes of standard and serially freezing these into a mold. The resulting tissue plug is then sectioned alongside the target tissue and mounted to the same sample target. Weighted linear regression can then be applied to correlate the average ion intensity of each layer of the model to its corresponding final tissue concentration. Reproduced with permission from Reference 54 © Creative Commons License Attribution 4.0 International (CC BY 4.0) (2009) https://creativecommons.org/licenses/by/4.0/

Figure 5. Simplified scheme of high-speed TOF/TOF system for acquisition of multiple TOF/TOF events in a single laser shot. a) Ions enter instrument and are separated with respect to *m/z* in TOF-1. b) The ion gate is opened to allow passage of first ion (blue) into the collision cell. c) Ion gate closes to prevent second ion (yellow) entrance into collision cell, while first ion (blue) and its fragments enter the reacceleration zone. d) The ion gate once again opens to allow the third ion (red) passage into the collision cell, as the first ion (blue) and its fragments are reaccelerated into TOF-2. e) The third ion (red) and its fragments enter the reacceleration zone and while the first ion (blue) and its fragments are separated with respect to *m/z* in TOF-2. d)The third ion (red) and its fragments are reaccelerated into the TOF-2 region. g) A combined spectrum

of both the first (blue) and third (red) ion and their respective fragments is obtained. The combined MS/MS spectra from a single laser shot allows normalization of analyte signal to standard signal with lower shot-to-shot variability. Figure reproduced with permission from Reference 60. Copyright (2016) American Chemical Society.

Figure 6. Quantification of fluvoxamine via on tissue derivatization with DPP-TFB. a) Different concentrations of fluvoxamine ranging from 0.02 mg/mL to 0.032 µg/mL using a dilution factor of 5 spotted on control tissue sections previously sprayed with D_4-fluvoxamine. b) Calibration curve using different intensity ratios of fluvoxamine/ D_4-fluvoxamine at different concentrations of fluvoxamine from a). c) DPP-TFB derivatized fluvoxamine in dosed tissue. d) Quantification of fluvoxamine in different regions of the brain. Cb: cerebellum, Cx: cortex, CP:caudate putamen, HIPP: hippocampus, TH: thalamus, VS: ventral striatum. Lateral scale bar is 2 mm. Intensity scale bar ranges are indicated on the right for a (0-5%) and c (0-40%). Figure reproduced with permission from Reference 70. Copyright (2018) American Chemical Society.

Figure 7. Another innovative strategy involving labeling with antibodies conjugated with gold nanoclusters (AuNC) has been introduced to enable quantitative MSI of the metallothionein protein with high sensitivity and accuracy. Figure reproduced with permission from Reference 89. Copyright (2018) American Chemical Society.

9. TERMS AND DEFINITIONS

1. **Mass spectrometry imaging (MSI):** an analytical technique, which enables direct label-free spatial analysis of hundreds of molecules in biological samples by measuring their abundances at different locations in the sample.
2. **Absolute quantification:** Determination of the exact amount or concentration of an analyte of interest in a sample.
3. **Relative quantification:** Determination of the relative change in an analyte concentration within or between the samples.
4. **Matrix effects:** Signal suppression or enhancement during ionization of complex mixtures due to competition for charge or differences in the efficiency of charged adduct formation.
5. **Internal standard:** A molecule added to the sample for quantification experiments, which accurately represents signal variations during ionization and transfer of analytes to a mass spectrometer.
6. **Matrix-assisted laser desorption ionization (MALDI):** an ionization technique, in which a light-absorbing matrix is deposited onto the sample to assist desorption and ionization of molecules with minimal fragmentation by interaction with a laser.
7. **Laser ablation (LA):** a technique, in which molecules are ablated from the sample by a laser.
8. **Desorption electrospray ionization (DESI):** an ambient ionization technique, in which molecules are removed from a sample by a stream of charged solvent droplets and ionized with minimal fragmentation.
9. **Nanospray desorption electrospray ionization (Nano-DESI):** an ambient ionization technique, in which molecules are extracted from a sample into a dynamic liquid bridge formed between two capillaries positioned at an angle and ionized by electrospray or nanospray ionization.
10. **Liquid extraction surface analysis (LESA):** an ambient ionization technique, in which molecules extracted from a sample into a static solvent droplet are subsequently transferred to a mass spectrometer inlet and ionized by nanospray ionization.
11. **Liquid microjunction surface sampling probe (LMJ-SSP):** a sampling probe composed of two coaxial capillaries, in which a solvent is delivered through the outer capillary and aspirated through the inner capillary thereby forming a liquid microjunction with the sample for direct analyte extraction.
12. **Total ion current (TIC) normalization:** a normalization method, in which each peak abundance in the mass spectrum is divided by the sum of abundances of all the peaks.
13. **Tissue extraction coefficient (TEC):** a ratio of the mean signal intensity of the analyte in a selected region of the tissue to its signal obtained off the tissue (e.g. on a glass slide). TEC is also referred to as signal extinction coefficient (SEC).
14. **Inductively coupled plasma mass spectrometry (ICP-MS):** a technique, in which the sample is atomized and ionized in a plasma generated in argon by an oscillating high-frequency electromagnetic field.
15. **Elemental fractionation:** a differential loss of certain elemental and molecular components due to processes occurring in the ablation plume, which alters the relative abundance of peaks in the mass spectrum.

16. **Mimetic tissue model:** a simplified model of a real tissue prepared from a tissue homogenate spiked with known concentrations of internal standards; the model helps to account for matrix effects and enables quantification.

Figure 1. An optical image of an MCAO brain tissue section with the ischemic region marked in pink and white matter marked in cyan (*top*). Ion images of $[M + Na]^+$ and $[M + K]^+$ of the PC 43:6 standard and endogenous PC 34:1 and PC 38:4. Ion images normalized to the TIC and PC 25:0 standard are denoted with "Norm TIC" and "Norm Std", respectively. Lateral scale bar is 2 mm. Intensity scale bar ranges from 0 (black) to 100% (light yellow) signal intensity of an individual peak. Figure adapted from Reference 36. Reproduced by permission of The Royal Society of Chemistry

[**Note to Annual Reviews: I am an author of this article; the publisher grants authors the right to reuse their own figures without permission.**]

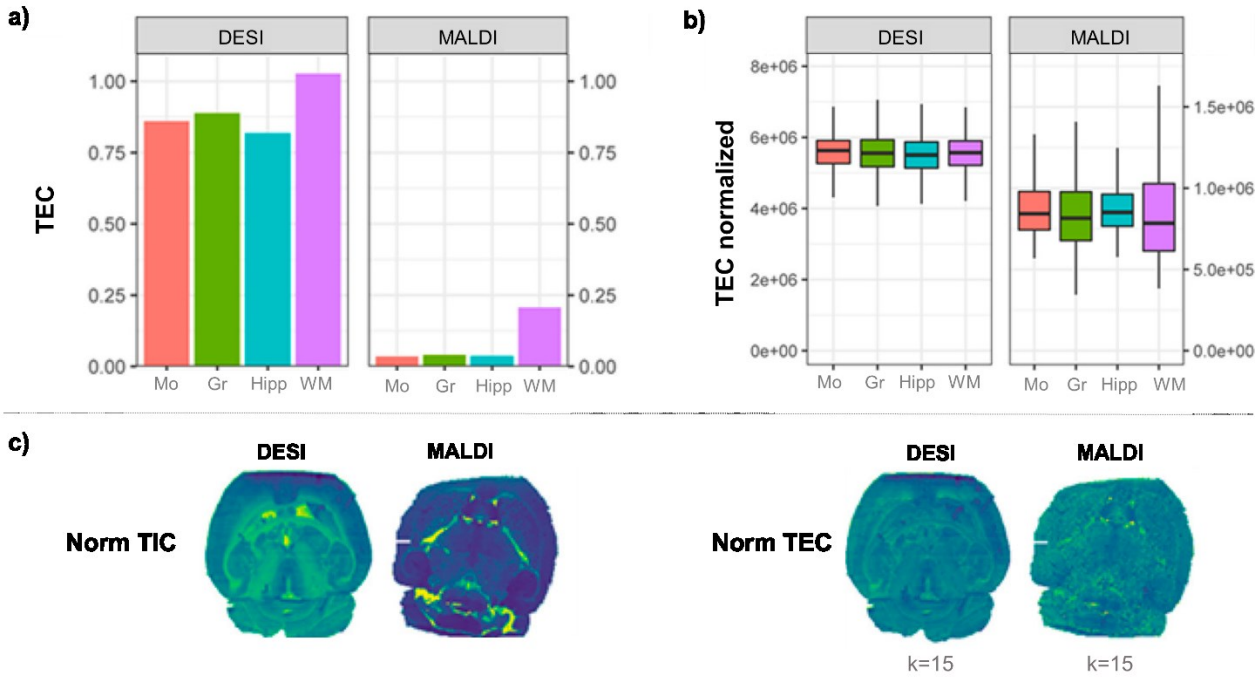

Figure 2. a) TEC and **b)** normalized TEC values calculated in DESI (left) and MALDI (right) for olanzapine as $[M + H]^+$ adduct (*m/z* 313.14) deposited on 10 µm mouse brain sections. Anatomical regions corresponding to the molecular (Mo) and granular (Gr) layers of the cerebellum, hippocampus (Hipp), and white matter (WM), which were successfully segmented using the graph-cuts clustering, are indicated with different color bars. **c)** Normalized TIC ion images of protonated olanzapine obtained with DESI and MALDI are shown in the left panel whereas normalized ion images of protonated olanzapine by cluster specific TECs are shown in the right panel for 15 clusters. Figure adapted with permission from Reference 40. Copyright (2018) American Chemical Society.

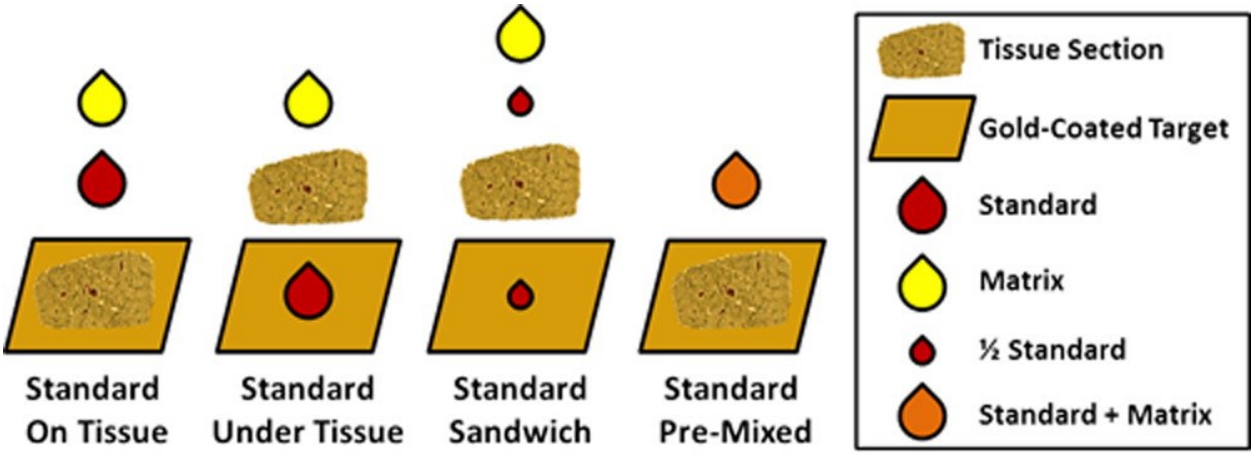

Figure 3. Illustration of the four methods of applying standards for IMS. Depositing the standards on the tissue section requires thaw-mounting the section followed by application of the standards and matrix. Deposition under the tissue section requires spotting the standards first, thaw-mounting the section on top of them, and then applying matrix. A sandwich method combines depositing the standards under and on the tissue section followed by matrix. Premixing the standard involves thaw-mounting the tissue section followed by depositing the standards and the matrix in a single solution. Figure reproduced with permission from Reference 52. Copyright (2016) American Chemical Society.

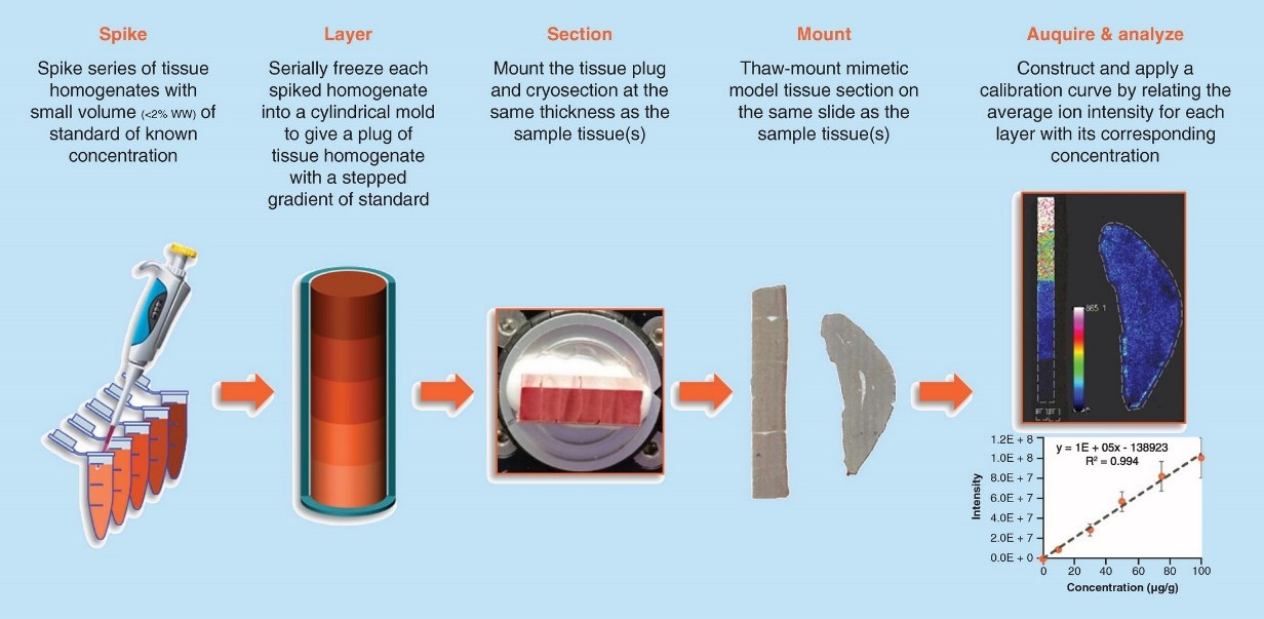

Figure 4. Schematic outlining the workflow for the generation and application of a mimetic tissue model for QMSI. The process involves spiking tissue homogenates with low volumes of standard and serially freezing these into a mold. The resulting tissue plug is then sectioned alongside the target tissue and mounted to the same sample target. Weighted linear regression can then be applied to correlate the average ion intensity of each layer of the model to its corresponding final tissue concentration. Reproduced with permission from Reference 54 © Creative Commons License Attribution 4.0 International (CC BY 4.0) (2009) https://creativecommons.org/licenses/by/4.0/

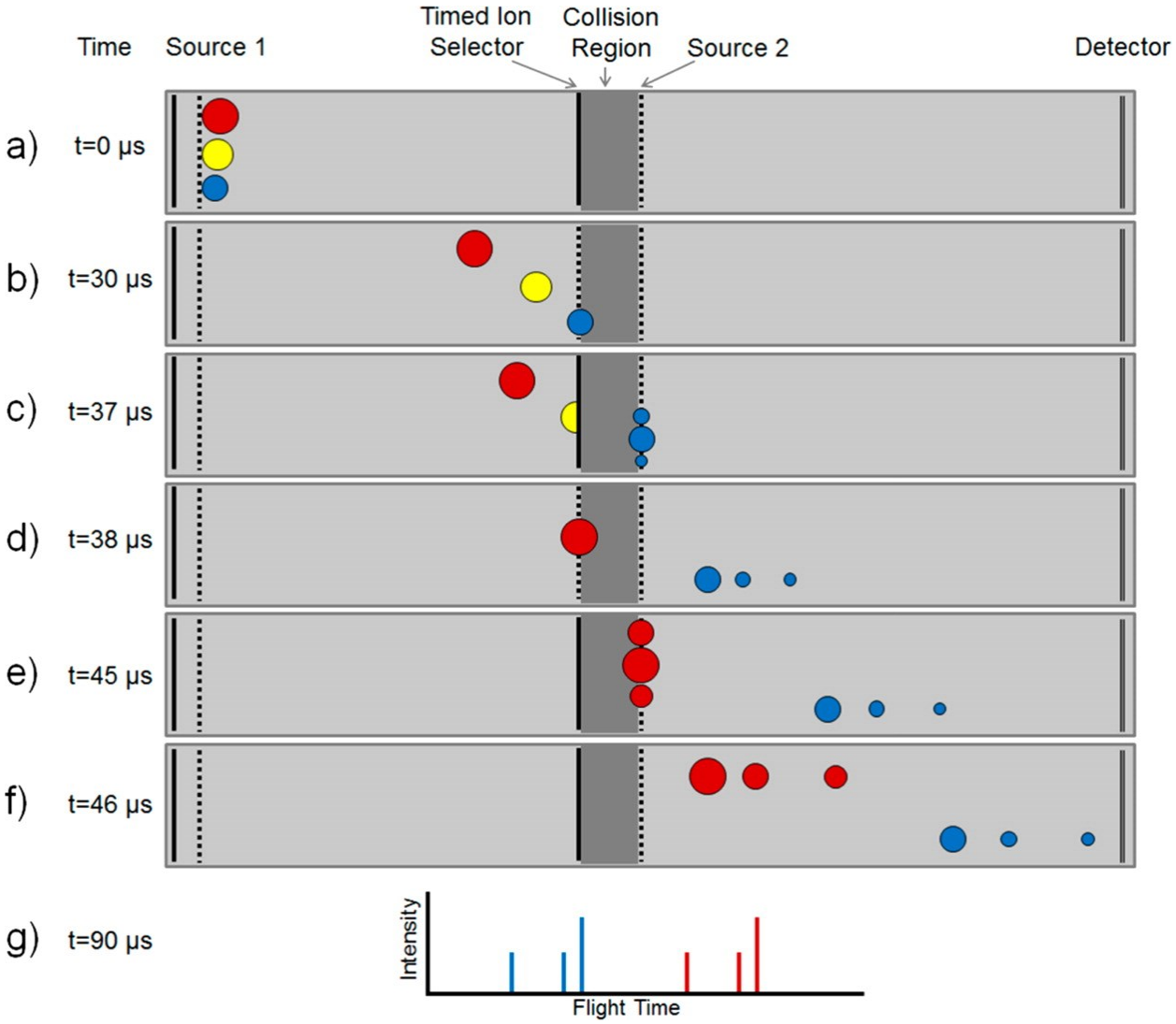

Figure 5. Simplified scheme of high-speed TOF/TOF system for acquisition of multiple TOF/TOF events in a single laser shot. a) Ions enter instrument and are separated with respect to *m/z* in TOF-1. b) The ion gate is opened to allow passage of first ion (blue) into the collision cell. c) Ion gate closes to prevent second ion (yellow) entrance into collision cell, while first ion (blue) and its fragments enter the reacceleration zone. d) The ion gate once again opens to allow the third ion (red) passage into the collision cell, as the first ion (blue) and its fragments are reaccelerated into TOF-2. e) The third ion (red) and its fragments enter the reacceleration zone and while the first ion (blue) and its fragments are separated with respect to *m/z* in TOF-2. d)The third ion (red) and its fragments are reaccelerated into the TOF-2 region. g) A combined spectrum of both the first (blue) and third (red) ion and their respective fragments is obtained. The combined MS/MS spectra from a single laser shot allows normalization of analyte signal to standard signal with lower shot-to-shot variability. Figure reproduced with permission from Reference 60. Copyright (2016) American Chemical Society.

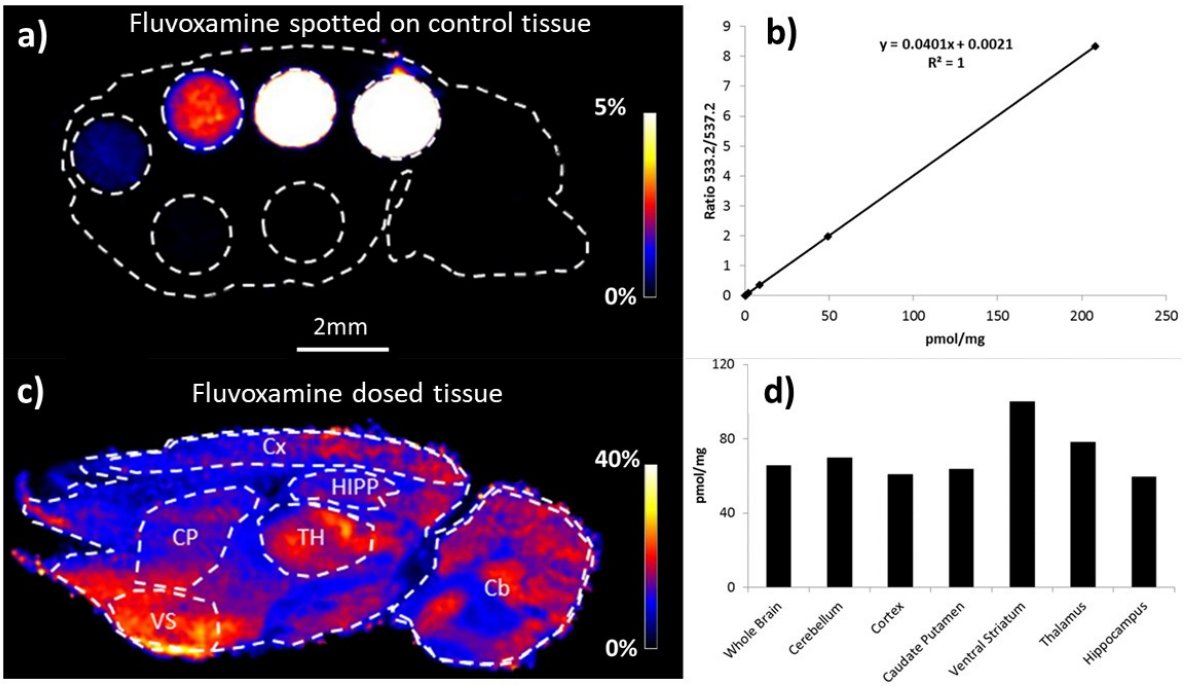

Figure 6. Quantification of fluvoxamine via on tissue derivatization with DPP-TFB. a) Different concentrations of fluvoxamine ranging from 0.02 mg/mL to 0.032 µg/mL using a dilution factor of 5 spotted on control tissue sections previously sprayed with D_4-fluvoxamine. b) Calibration curve using different intensity ratios of fluvoxamine/ D_4-fluvoxamine at different concentrations of fluvoxamine from a). c) DPP-TFB derivatized fluvoxamine in dosed tissue. d) Quantification of fluvoxamine in different regions of the brain. Cb: cerebellum, Cx: cortex, CP:caudate putamen, HIPP: hippocampus, TH: thalamus, VS: ventral striatum. Lateral scale bar is 2 mm. Intensity scale bar ranges are indicated on the right for a (0-5%) and c (0-40%). Figure reproduced with permission from Reference 70. Copyright (2018) American Chemical Society.

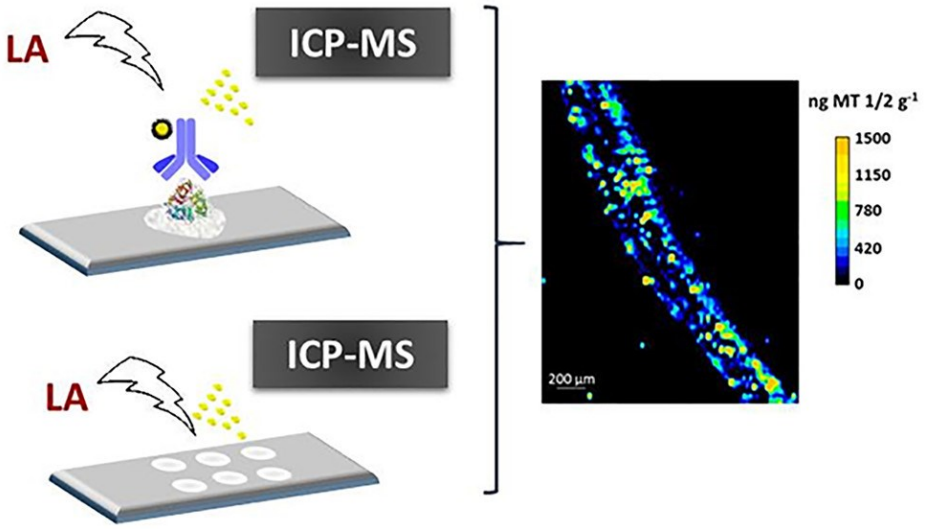

Figure 7. Another innovative strategy involving labeling with antibodies conjugated with gold nanoclusters (AuNC) has been introduced to enable quantitative MSI of the metallothionein protein with high sensitivity and accuracy. Figure reproduced with permission from Reference 89. Copyright (2018) American Chemical Society.